Article

The Influence of Boron and Carbon Addition on the Glass Formation and Mechanical Properties of High Entropy (Fe, Co, Ni, Cr, Mo)-(B, C) Glassy Alloys

Fanli Kong [1], Akihisa Inoue [1,2,*], Fang Wang [2,*] and Chuntao Chang [2]

[1] Innovation Base, Josai International University, Togane 283-8555, Japan; kong@jiu.ac.jp
[2] School of Mechanical Engineering, Dongguan University of Technology, Dongguan 523808, China; changct@dgut.edu.cn
[*] Correspondence: inoue@jiu.ac.jp (A.I.); wangfang917@126.com (F.W.)

Abstract: Coatings made from metallic glasses are a promising solution for protecting surfaces of materials in various challenging environments. From an engineering perspective, glassy alloy coatings containing carbon are of greater importance compared to those without carbon but containing boron. Despite anticipating improved coating characteristics, there is no data on using high entropy glassy alloy as a coating material. In this paper, we investigated the influence of the simultaneous addition of boron and carbon elements on the glass-forming ability, thermal stability, crystallization behavior, yield strength, hardness, and corrosion resistance of high entropy (Fe, Co, Ni, Cr, Mo)-(B, C) glassy alloys. It was found that the content of boron and carbon had a significant effect on the improvements of glass-forming ability, mechanical properties, and corrosion resistance. The $(Fe_{0.25}Co_{0.25}Ni_{0.25}Cr_{0.125}Mo_{0.125})_{75}(B_{0.7}C_{0.3})_{25}$ bulk glassy alloy exhibits high glass-forming ability, high yield strength of 3500 MPa, Vickers hardness of 1240, and the highest corrosion resistance among the alloys. We also discussed the reason for their good engineering properties, and the possibility of using high entropy glassy alloys as coating materials, in addition to the guidelines for designing high-performance multicomponent glassy alloys.

Keywords: metallic glasses; high-entropy alloy; high thermal stability; corrosion resistance

1. Introduction

High-entropy bulk metallic glasses (HE-BMG) are a kind of glasses that inherit unique properties of both high-entropy alloys (HEA) and bulk metallic glasses (BMG), such as high thermal stability, superior mechanical, and magnetic properties [1–3]. They are composed of five or more elements in equal or near-equal atomic percent, which have relatively high mixing entropy compared with conventional metallic glasses based on a single principal element [3–5]. They also exhibit new structures and phenomena induced by high entropy effort that can form glassy structures with low cooling rates and extremely stable glassy phase to crystallization due to slow atomic diffusion and the glassy structure with medium-range order (MRO) atomic configurations containing coexistent atomic pair with positive and negative heat of mixing [6–8].

The glass transition phenomenon before crystallization was found in Au-Si-Ge amorphous alloy in 1970, which can be identified as the first report on a glassy type of alloy [9]. Twenty years later, Mg- and La-based BMGs without any noble metals were synthesized by copper mold casting and a new type of material age was created, leading to the present active research and application states of BMGs and multicomponent alloys [10–12]. Since then, various types of metallic glasses have been developed successively and most of the glassy alloys contain a main component element with concentrations of over 40 at.%, which is called the base element [12]. With the aim of developing BMGs without a dominant element and examining the influence of high-order multicomponent pairs, Ma et al. used

equal amounts of five elements—Ti, Zr, Hf, Cu, and Ni—and successfully synthesized a new kind of equiatomic glassy alloy composed of $Ti_{20}Zr_{20}Hf_{20}Cu_{20}Ni_{20}$ with a diameter of 1.5 mm in 2002 [4], which is the first report on high entropy alloy (HEA) and HE-BMG. Afterward, half of Pd was replaced with Pt in $Pd_{40}Cu_{20}Ni_{20}P_{20}$ BMG, and an equiatomic $Pd_{20}Pt_{20}Cu_{20}Ni_{20}P_{20}$ HE-BMG with a maximum diameter of 10 mm was fabricated by fluxed water quenching in 2011 [12]. Since then, many researchers have explored the possibility of synthesizing high entropy BMGs with various combinations of elements and methods, such as Ti-Zr-Cu-Ni-Be [13], Zr-Hf-Ti-Cu-Ni-Co-Al [14], Fe-Co-Ni-B-Si [15], Er-Gd-Y-Al-Co [16], Ti-Zr-Hf-Be-Cu-Ni [17], and the recently developed pseudo high entropy (PHE) BMGs [18], such as Zr-Al-Ni-Cu-Au [19] and Zr-Fe-Ni-Si-B [20]. They are considered a promising material for exploring the nature of glass and designing novel materials for structures and coatings that are strong, flexible, and can withstand corrosion, wear, and erosion [1,2,17,21,22].

When we look at the use of BMGs as a coating material, there are some previous papers that exhibit useful characteristics such as high hardness, high corrosion resistance, high wear resistance, and high heat resistance strength [23]. Owing to these useful properties, the Fe-Cr-Mo-B-C BMG coating on stainless steel has been used as a practical material for vessels with a diameter of 30–50 cm for lead-free soldering liquid which requires simultaneously high corrosion resistance, high heat-resistant strength, and high heat-resistant oxidation resistance, etc. [12,24]. The thickness of the surface coating layer reaches about 0.3 mm and no appreciable voids can be observed. It is well known that high entropy-type BMGs can have lower atomic diffusivity, higher hardness, good corrosion resistance, and higher heat resistance strength. However, there has been no data on the use of HE-BMGs as a coating material, in spite of the expectation of obtaining better coating characteristics. With the aim of clarifying the usefulness of HE-BMGs as a coating material, this paper intends to examine the fundamental properties of HE (Fe, Co, Ni, Cr, Mo)-(B, C) glassy alloys, which can be regarded as a further multiplication of the previous Fe-based glassy coating material.

2. Materials and Methods

The multicomponent alloy ingots with nominal atomic compositions of $(Fe_{0.25}Co_{0.25}Ni_{0.25}Cr_{0.125}Mo_{0.125})_{100-x}(B_{0.7}C_{0.3})_x$ (x = 15, 17.5, 18.5, 20, 22.5 and 25 at.%) were prepared by arc-melting the mixtures of pure Fe, Co, Ni, Cr, and Mo metals, crystal boron and Fe_3C alloy with purities above 99.8 wt.% under an argon atmosphere [25,26], and the alloys were melted and solidified for more than 3 cycles to ensure the homogeneity of the alloy ingot. The specimens used for the present study were in ribbon form with a thickness of about 30 μm, a width of about 1.5 mm by the single roller melt spinning method with a circumferential velocity of 35 m/s, and in rod form with an outer diameter of 2 mm by copper mold casting in an argon atmosphere. The structures of the as-quenched and annealed ribbon and rod samples were measured by X-ray diffraction (XRD, Miniflex 600, Rigaku, Tokyo, Japan) with Cu Kα radiation. Differential scanning calorimetry (DSC, METTLER TOLEDO TGA/DSC1/1600, METTLER TOLEDO, Columbus, OH, USA) was used to investigate the thermal stability related to the glass transition, supercooled liquid area, and crystallization at a heating rate of 0.67 K/s. A Vickers hardness indenter (Wilson Hardness Tukon 1202, Wilson, Tokyo, Japan) was used to assess the hardness of the rod sample with a 0.98 N load. Slip markings around Vickers hardness indents were examined by scanning electron microscopy (SEM, JEOL JSM-IT800, JEOL, Tokyo, Japan). The mechanical characteristics of Young's modulus, yield strength, fracture strength, and fracture strain were investigated at room temperature in a uniaxial compressive deformation mode using an Instron-style testing apparatus. The sample's dimensions were 2 mm in height and 2 mm in diameter, and the starting strain rate was 5×10^{-4}/s. The samples were degreased, washed, and dried in air before immersion in 3 mass% NaCl solution at 298 K for evaluating the corrosion behavior by electrochemistry test.

3. Results

Figure 1 shows the (a) XRD patterns and (b) DSC curves of the as-spun $(Fe_{0.25}Co_{0.25}Ni_{0.25}Cr_{0.125}Mo_{0.125})_{100-x}(B_{0.7}C_{0.3})_x$ (x = 15, 17.5, 18.5, 20, 22.5, 25 at.%) ribbons. All the XRD patterns are characterized by the absence of sharp peaks, which means the lack of long-range ordered structure. Instead, the patterns consist of amorphous diffraction halos, indicating the formation of only an amorphous phase. The top position of the halos shifts to a lower angle with increasing B and C content, as arrowed in Figure 1a, indicating that the average nearest-neighbor atomic spacing in the amorphous phase increases [25]. This phenomenon is opposite to the trend for C-free $(Fe_{0.25}Co_{0.25}Ni_{0.25}Cr_{0.125}Mo_{0.125})_{100-x}B_x$ glassy alloys, where the first shell neighbor atomic distance of the component atoms decreases as the B concentration increases. The distinct difference indicates that the first shell neighbor distance is significantly affected by the presence of carbon, which is probably due to the competitive relationship between (ETM, LTM)-B and (ETM, LTM)-C local short-range-order formation. As is shown in Figure 1b, the onset temperature of the first exothermic peak (T_{x1}) increases from 734 K to 860 K, and the glass transition phenomenon becomes more significant with increasing B and C contents, indicating the glassy phases are formed for the alloys. For the x = 25 alloy, the shape and area of the first exothermic peak are noticeably different from those for alloys with lower B and C contents. To investigate the reason for this phenomenon, we studied the crystallization behavior of the alloys.
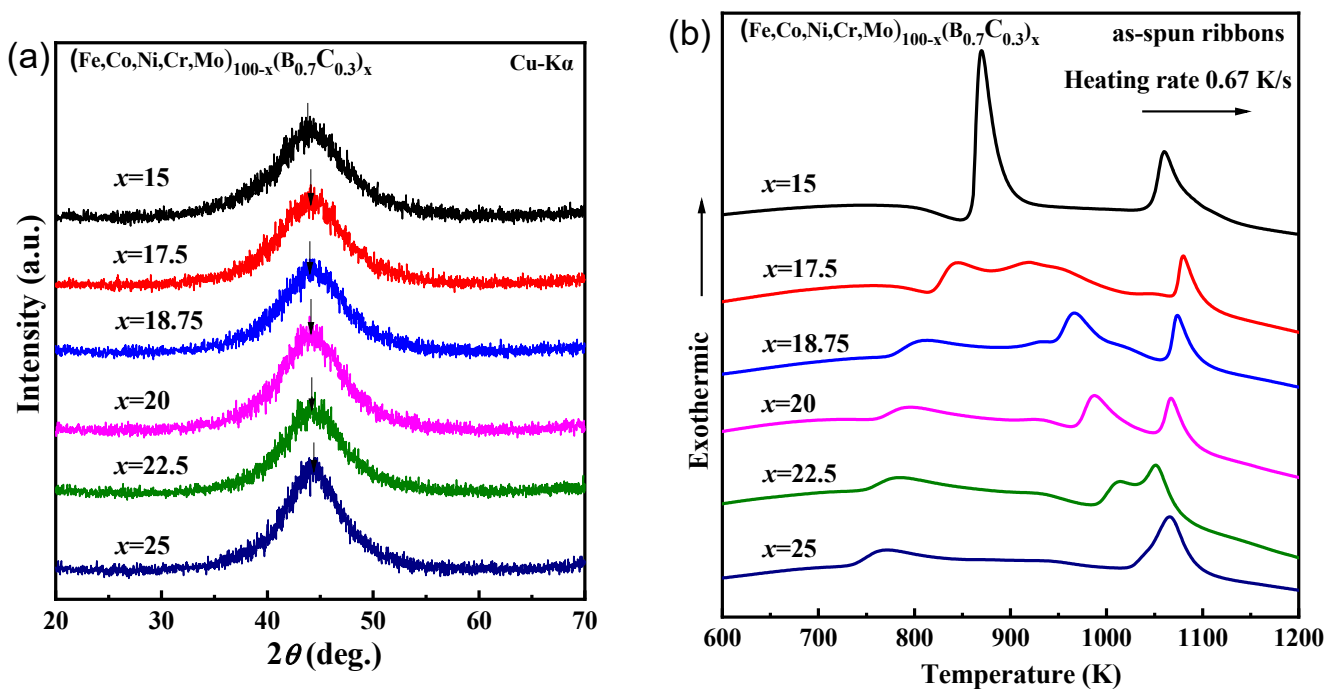

Figure 1. (**a**) X-ray diffraction (XRD) patterns and (**b**) differential scanning calorimetry (DSC) curves of the as-spun $(Fe_{0.25}Co_{0.25}Ni_{0.25}Cr_{0.125}Mo_{0.125})_{100-x}(B_{0.7}C_{0.3})_x$ (x = 15, 17.5, 18.5, 20, 22.5, 25 at.%) ribbons.

Figure 2a shows the XRD patterns of as-spun the $(Fe_{0.25}Co_{0.25}Ni_{0.25}Cr_{0.125}Mo_{0.125})_{100-x}(B_{0.7}C_{0.3})_x$ alloys annealed for 1800 s at each first exothermic peak temperature (T_{p1}). It is noticed that the glassy structure has been largely retained, with only a small amount of face-centered cubic (FCC) crystalline structure precipitated for alloys with B and C contents of 15%–22.5%, despite the rather long annealing time. The formation of an extremely stable glassy phase to crystallization is also found in a type of pseudo high entropy (PHE) glassy alloys [20,27]. The remarkably elevated resistance to crystallization can be attributed to the glassy structure, which consists of uniquely coexisting two types of MRO atomic configurations, including one type of MRO characterized by the presence of atomic pairs with positive heat of mixing, and another type of MRO exclusively comprised of negative atomic pairs [27]. In contrast, for the alloy with a B and

C content of 25%, the crystallization of the $M_{23}B_6$ phase from the amorphous phase has almost completed. This result is consistent with Figure 1 that the alloys with higher B and C content possess a more loosely packed atomic structure. Figure 2b shows the XRD patterns of $(Fe_{0.25}Co_{0.25}Ni_{0.25}Cr_{0.125}Mo_{0.125})_{80}(B_{0.7}C_{0.3})_{20}$ amorphous alloys annealed for 1800 s at 803 K, 966 K, and 1093 K, corresponding to the three exothermic peak temperatures. It is concluded that the crystallization of the FCC phase, $M_{23}B_6$, and $Co(MoB)_2$ phases corresponds to the first, second, and third peaks, respectively. The crystallization process is as follows: [am] → [am′ (remaining amorphous) + FCC] → [am″ + FCC + $M_{23}B_6$] → [FCC + $M_{23}B_6$ + $Co(MoB)_2$]. Remarkably, the presence of [amorphous + FCC] phases extends across an exceptionally broad temperature interval, ranging from 800 to 960 K.
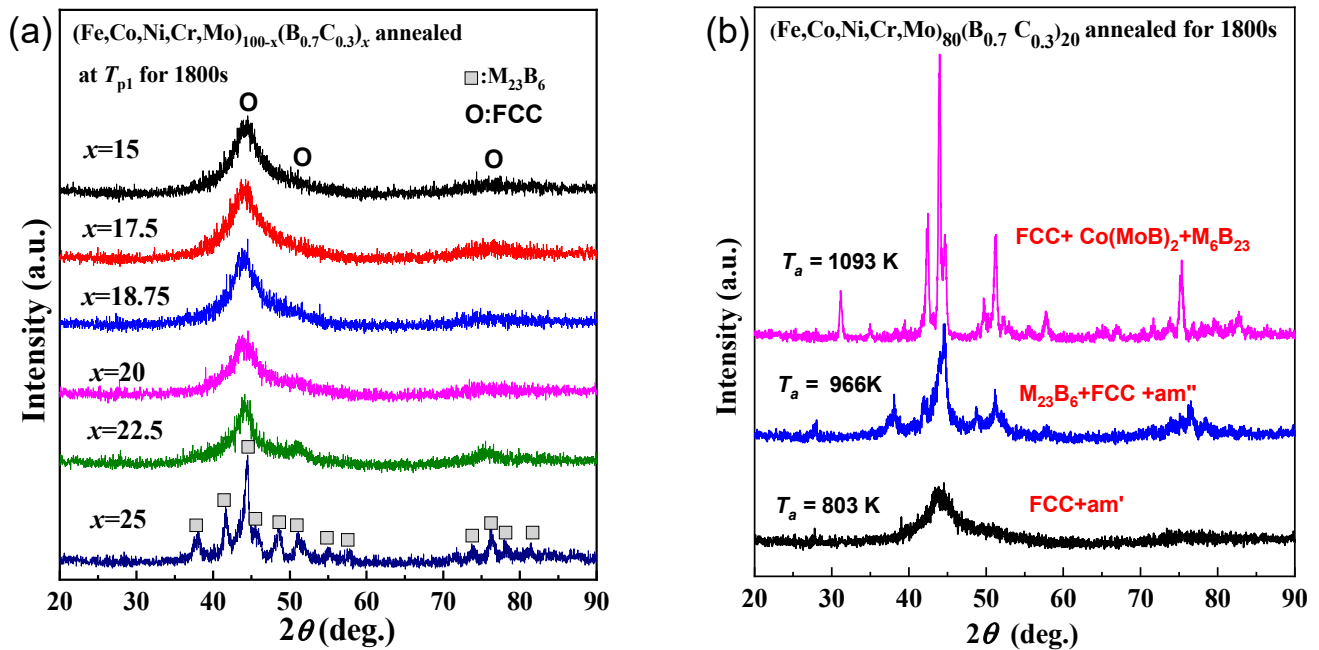
Figure 2. (**a**) XRD patterns of the $(Fe_{0.25}Co_{0.25}Ni_{0.25}Cr_{0.125}Mo_{0.125})_{100-x}(B_{0.7}C_{0.3})_x$ (x = 15, 17.5, 18.5, 20, 22.5, 25 at.%) alloys annealed for 1800 s at each first exothermic peak temperature (T_{p1}) of these as-spun glassy alloys. (**b**) XRD patterns of as-spun $(Fe_{0.25}Co_{0.25}Ni_{0.25}Cr_{0.125}Mo_{0.125})_{80}(B_{0.7}C_{0.3})_{20}$ alloy annealed for 1800 s at 803 K, 966 K and 1093 K, corresponding to the three exothermic peak temperatures.

The as-cast rods with a diameter of 2 mm were prepared for the x = 17.5–25 alloys. As is shown by the XRD patterns in Figure 3a, only the alloy with x = 25 shows a glassy phase, while the alloys with x = 17.5–20 show the precipitation of FCC phase, and additionally, the alloy with x = 17.5 shows an extra precipitation of $Co(MoB)_2$ phase. The DSC curves of the as-cast rod samples are shown in Figure 3b. The x = 25 rod alloy shows almost the same crystalline behavior as the ribbon sample. However, the x = 17.5–20 alloys do not show the first exothermic peaks. As is shown in Figure 4a,b, only a portion near the outer periphery of the cylinder formed a glassy structure due to the low cooling rate and low glass-forming ability. Therefore, the first exothermic peak is almost invisible because of the low glassy content.
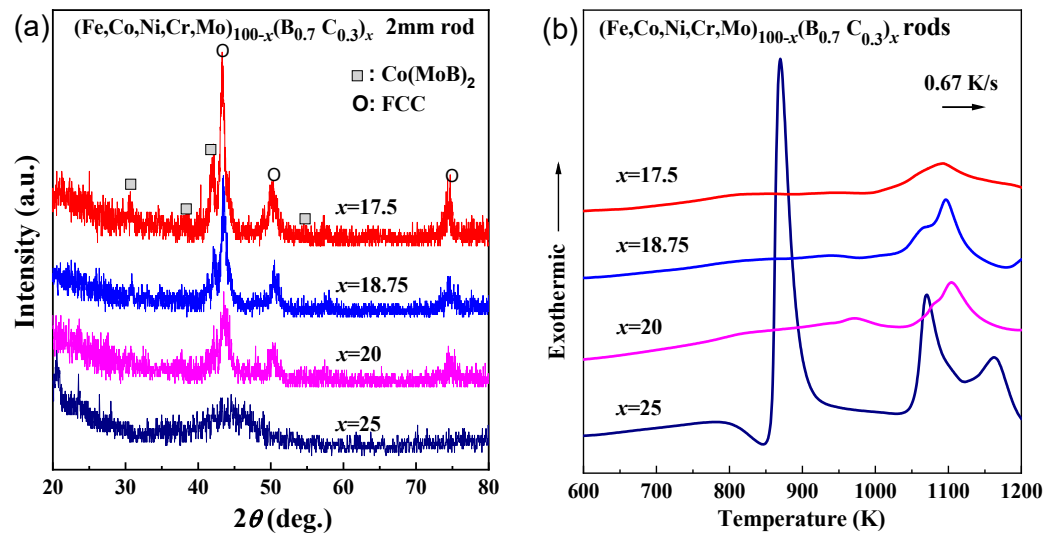
Figure 3. (**a**) XRD patterns and (**b**) DSC curves of the as-quenched $(Fe_{0.25}Co_{0.25}Ni_{0.25}Cr_{0.125}Mo_{0.125})_{100-x}(B_{0.7}C_{0.3})_x$ ($x = 17.5$, 18.5, 20 and 25 at.%) rods with a diameter of 2 mm.
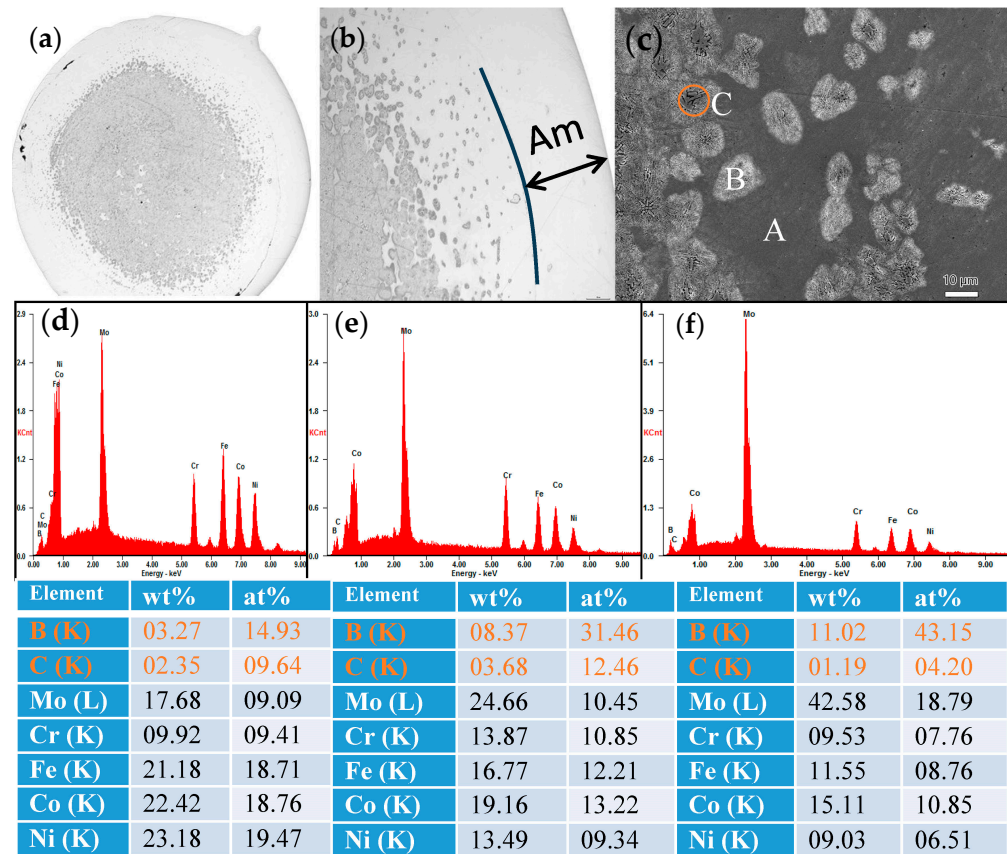

Element	wt%	at%
B (K)	03.27	14.93
C (K)	02.35	09.64
Mo (L)	17.68	09.09
Cr (K)	09.92	09.41
Fe (K)	21.18	18.71
Co (K)	22.42	18.76
Ni (K)	23.18	19.47

Element	wt%	at%
B (K)	08.37	31.46
C (K)	03.68	12.46
Mo (L)	24.66	10.45
Cr (K)	13.87	10.85
Fe (K)	16.77	12.21
Co (K)	19.16	13.22
Ni (K)	13.49	09.34

Element	wt%	at%
B (K)	11.02	43.15
C (K)	01.19	04.20
Mo (L)	42.58	18.79
Cr (K)	09.53	07.76
Fe (K)	11.55	08.76
Co (K)	15.11	10.85
Ni (K)	09.03	06.51

Figure 4. The SEM images of (**a**) $(Fe_{0.25}Co_{0.25}Ni_{0.25}Cr_{0.125}Mo_{0.125})_{80}(B_{0.7}C_{0.3})_{20}$ alloy in rod form with a diameter of 2 mm, (**b**) the magnification of the transition zone and (**c**) further magnification of the transition zone. Energy Dispersive X-ray (EDX) spectroscopy profile of the selected area of (**d**) A (**e**) B and (**f**) C in (**c**), respectively. The corresponding compositions in weight and atomic percentage are shown under the figure.

To illustrate the microstructure of the $(Fe_{0.25}Co_{0.25}Ni_{0.25}Cr_{0.125}Mo_{0.125})_{80}(B_{0.7}C_{0.3})_{20}$ alloy rod, the SEM images are presented in Figure 4a–c. As can be seen from Figure 4a,b, the region near the outer periphery of the cylinder is amorphous. As it moves towards the

center position of the cylinder, there is a gradual transition from the amorphous phase to a region where amorphous and crystalline phases coexist, and finally to a region comprising entirely crystalline structures. As shown in Figure 4c, in addition to the amorphous phase labeled as region *A*, there are two types of crystal phases, labeled as region B and C. In order to elucidate the composition of regions A, B, and C, Energy Dispersive X-ray (EDX) spectroscopy profiles are presented in Figure 4d–f, respectively. The composition of region A is close to the original alloy composition, although the carbon content is higher, indicating it can be identified as the remaining amorphous phase after crystal precipitation. In region B, there is an increase in boron, chromium, and molybdenum contents, while in region C, the boron content further elevates, suggesting the presence of $Co(Mo, B)_2$ phase. This component redistribution behavior is in accordance with the results obtained from XRD analysis in Figure 3.

Figure 5a–c show the change in Vickers hardness along the central axis of the cross-section of the rod sample with a diameter of 2 mm. It can be observed that the hardness at the internal center of the cylinder is generally consistent with that in the outer peripheral regions in Figure 5a, indicating the high glass-forming ability of the $x = 25$ alloy and the uniformity of the glassy structure. In contrast, the hardness at the internal center of the rod is notably lower than that of the region closer to the periphery, corresponding to the difference in the cooling rates between the inside and outside regions of the rod, resulting in different structures. Although the hardness of the internal center region is generally lower than the hardness near the region closer to the periphery, there are some areas where the hardness is nearly the same as that of the region near the periphery, which indicates a coexistence of glassy and crystalline phases in Figure 5b. However, the hardness of the internal center region is much lower than the region near the outer edge, suggesting that the interior is entirely crystalline and does not form a glassy phase in Figure 5c. It should be noted that the hardness for the glassy and crystalline coexisting phases is higher than that of the amorphous phase and has the following relationship: $Hv_{am} < Hv_{am+FCC} < Hv_{FCC+Boride}$.

To validate this relationship between hardness and phase, we conducted annealing on the $(Fe_{0.25}Co_{0.25}Ni_{0.25}Cr_{0.125}Mo_{0.125})_{80}(B_{0.7}C_{0.3})_{20}$ ribbon sample. The phases and hardness of the alloy with different annealing temperatures are shown in Figure 5d. At the quenched state, the hardness is 1180 Hv. With an increase in annealing temperature, the precipitations of the FCC phase and borides occur, leading to a gradual increase in hardness up to 1670 Hv. After the precipitation of borides, further increases in the annealing temperature result in a reduction in hardness due to grain growth and coarsening. It can be observed that the hardness relationship between different phases in the ribbon samples is consistent with the relationship observed in the rod-shaped samples.

Figure 6a shows the tensile stress–strain curves of the as-cast rods with a diameter of 2 mm for $(Fe_{0.25}Co_{0.25}Ni_{0.25}Cr_{0.125}Mo_{0.125})_{100-x}(B_{0.7}C_{0.3})_x$ ($x = 15$, 17.5, 20 and 25) alloys. The fracture occurs without any noticeable prior change in the rate of elongation for all four samples, indicating the brittleness under tensile load. The glassy alloy with $x = 25$ shows the highest yield strength of 3500 MPa, while the alloy with $x = 20$ shows the lowest yield strength of 1830 MPa. Although the alloys are brittle under tension, nanoindentation load-depth curves show that the alloys are elastic–plastic-type and reveal plastic deformation under compression [28]. The hardness values at the center of the 2 mm rod samples with the different B and C contents are shown in Figure 6b. With increasing B and C contents from $x = 15$ to $x = 25$, the hardness increases from 1080 to 1240. The change is consistent with the above results of Figure 5a–c.
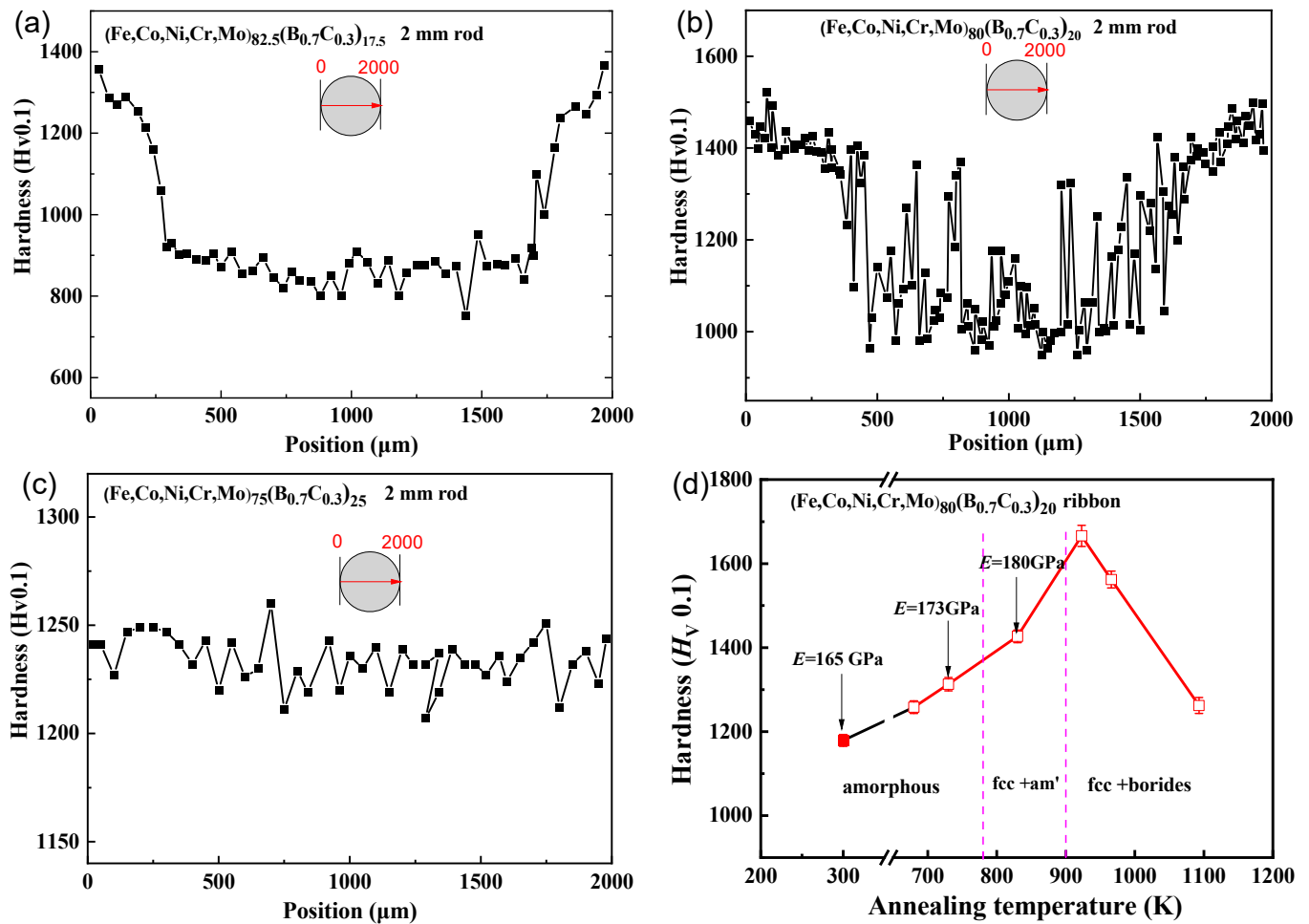
Figure 5. Vickers hardness of (**a**) (Fe$_{0.25}$Co$_{0.25}$Ni$_{0.25}$Cr$_{0.125}$Mo$_{0.125}$)$_{82.5}$(B$_{0.7}$C$_{0.3}$)$_{17.5}$, (**b**) (Fe$_{0.25}$Co$_{0.25}$Ni$_{0.25}$Cr$_{0.125}$Mo$_{0.125}$)$_{80}$(B$_{0.7}$C$_{0.3}$)$_{20}$, (**c**) (Fe$_{0.25}$Co$_{0.25}$Ni$_{0.25}$Cr$_{0.125}$Mo$_{0.125}$)$_{75}$(B$_{0.7}$C$_{0.3}$)$_{25}$ along the central axis of the cross-section rod sample with a diameter of 2 mm, and (**d**) the Vickers hardness (Fe$_{0.25}$Co$_{0.25}$Ni$_{0.25}$Cr$_{0.125}$Mo$_{0.125}$)$_{80}$(B$_{0.7}$C$_{0.3}$)$_{20}$ for the ribbon samples annealed from 680 K to 1093 K and the structure and Young's modulus are also shown.
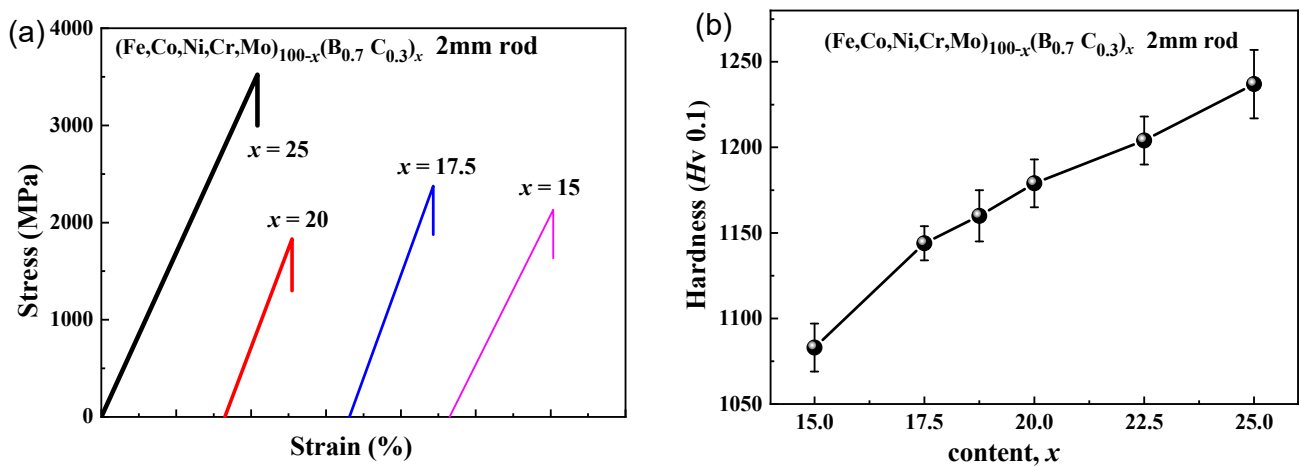
Figure 6. (**a**) Tensile stress-strain curves and (**b**) the changes of hardness of the as-cast rod with a diameter of 2 mm for (Fe$_{0.25}$Co$_{0.25}$Ni$_{0.25}$Cr$_{0.125}$Mo$_{0.125}$)$_{100-x}$(B$_{0.7}$C$_{0.3}$)$_x$ (*x* = 15–25) alloy.

Figure 7 illustrates the polarization curves of the alloys in ribbon form with *x* ranging from 15 to 25. It is observed that as the B and C contents increase, the curves shift towards

higher potential, suggesting that the increasing of B and C contents causes the reduction in the active energy of passivation, leading to an enhanced ease in attaining the passive state. The reason for the changes in corrosion characteristics will be discussed in the following section.
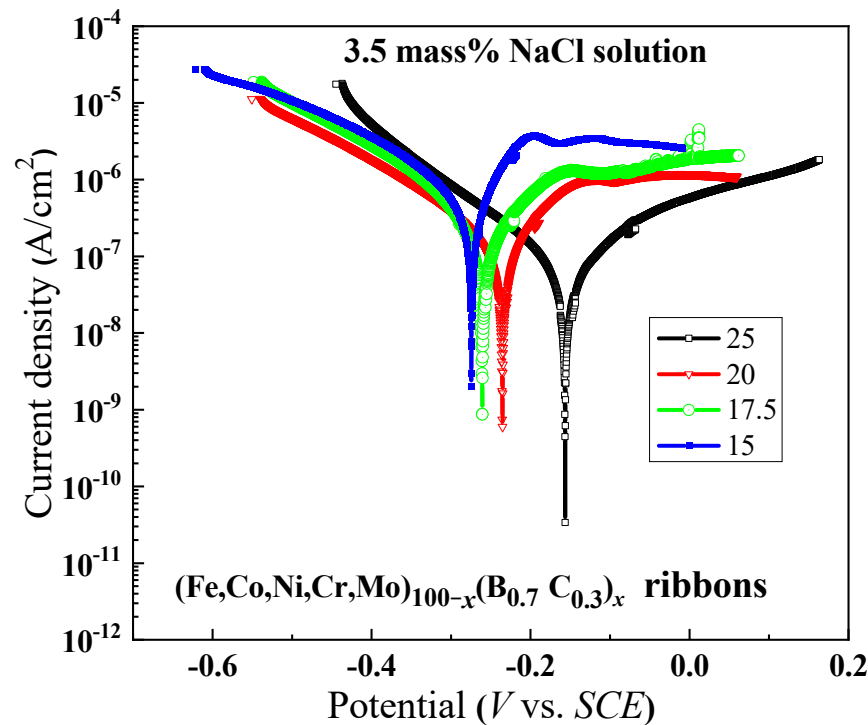
Figure 7. Polarization curves of $(Fe_{0.25}Co_{0.25}Ni_{0.25}Cr_{0.125}Mo_{0.125})_{100-x}(B_{0.7}C_{0.3})_x$ (x = 15, 17.5, 20 and 25) amorphous ribbons in 3.5 mass% NaCl aqueous solution at 298 K.

4. Discussion

The formation of the amorphous phase occurs in the range of x = 18–24 at.% for melt-spun alloys of $(Fe_{0.25}Co_{0.25}Ni_{0.25}Cr_{0.25})_{100-x}B_x$ [24], and this range significantly expands to 11–31 at.% for alloys of $(Fe_{0.25}Co_{0.25}Ni_{0.25}Cr_{0.125}Mo_{0.125})_{100-x}B_x$ [25,26], where the B-content range conducive to plasticity is also prolonged. In this paper, the simultaneous addition of B and C, of 25 at.% B and C, the BMG was formed with a diameter of 2 mm. The alloy rod shows a high yield strength of 3500 MPa, although no plastic deformation is exhibited. Also, the rod shows a high Vickers hardness of 1237 ± 20. The high strength and hardness are thought to result from the following: (1) the simultaneous addition of B and C elements promotes better microstructural homogeneity, reducing the likelihood of localized weaknesses. This overall improvement in material uniformity enhances its mechanical properties, including yield strength. (2) B and C atoms interact with the base metal atoms due to the strong attractive forces between them, as demonstrated by the large negative heats of mixing among them [8]. The interaction results in strong atomic clusters, which hinder the formation of shear bands and local rearrangement of atoms. This interaction increases the resistance of the material to plastic deformation.

The reasons for higher corrosion resistance with increasing B and C contents could probably be attributed to several factors, including: (1) The increasing of B and C can enhance the glass-forming ability of the alloy, thereby making the internal structure of the glassy phase more uniform, preventing the formation of crystalline phases that are more prone to corrosion. (2) B and C elements can form stable carbide and boride compounds, which are more chemically inert, acting as a barrier against corrosive agents [29]. (3) B and C elements can also increase the passivation potential and decrease the corrosion

current density of glassy alloys, which means they can make the alloys more resistant to electrochemical reactions that cause corrosion [30].

Here, we want to discuss the design of high-entropy glassy alloys. As is known, three empirical guidelines for the formation of BMGs are as follows [10]: (1) the alloy should be multicomponent, comprising a minimum of three elements; (2) there should be significant atomic size mismatches, exceeding approximately 12%, among the main elements; and (3) the main element pairs should exhibit negative heats of mixing. For high entropy alloys, although some authors have characterized alloys consisting of four components as high entropy alloys, the universally accepted definition is alloys with equal or relatively large proportions of five or more elements [5,31], usually exhibiting small atomic size mismatches below 5% and nearly zero heat of mixing. As multicomponent alloys, the number of the elements is well agreed with the first empirical guidelines. For the atomic size mismatching and heat of mixing, the constituent elements in high entropy bulk metallic glasses (HE-BMGs) are divided into two groups. For one group, the constituent elements have large atomic size mismatches exceeding 12% and significantly negative heats of mixing, consistent with the formation criteria for traditional BMGs. In contrast, the elements in the other group exhibit small atomic size mismatches below 5% and nearly zero heat of mixing, in alignment with the formation criteria for crystalline high-entropy alloys. As a result, HE BMGs exist in an intermediate state where component characteristics from both conventional BMGs and crystalline high-entropy alloys are combined.

Therefore, the HE-BMGs with the simultaneous presence of multiple elements in nearly equal proportions and the absence of a well-defined crystal structure, can be regarded as a class of advanced materials that combine the characteristics of HEAs with the glassy structure typical of metallic glasses. The design and development of high-entropy glassy alloys involve a balance of alloying elements and processing conditions to achieve the desired material properties while keeping the glassy structure. In the present alloy system, B and C elements are essential to improve the glass-forming ability and form the glassy structure for ribbon samples. With the increase in B and C contents to 25%, the 2 mm rod samples are fully glassy phase. The following possible benefits of using the present HE-BMGs as coating materials are encouraging: High thermal stability allows them to withstand high temperatures without crystallization, which is a crucial property for coatings used in high-temperature environments. Additionally, the HE-BMGs are good options for protective coatings in hostile situations due to their exceptional corrosion resistance. The high hardness makes them effective in providing protective coatings against abrasion. However, challenges such as processing techniques and cost-effectiveness need to be addressed for practical applications. Further research and development are necessary to optimize the properties of the HE-BMG coatings and ensure their successful application in various industries [32–34].

5. Conclusions

We examined the structure, thermal stability, mechanical properties, and corrosion resistance of the high entropy $(Fe_{0.25}Co_{0.25}Ni_{0.25}Cr_{0.125}Mo_{0.125})_{100-x}(B_{0.7}C_{0.3})_x$ (x = 15, 17.5, 18.5, 20, 22.5, 25) alloys in ribbon and rod forms, with the aim of clarifying the simultaneous addition effect of B and C elements. The results obtained are summarized as follows:

(1) The amorphous phase was formed in all ribbon alloys with x ranging from 15 to 25, but only in the rod with a diameter of 2 mm when x was 25.

(2) The crystallization process can be represented as $[am] \rightarrow [am' + FCC] \rightarrow [am'' + FCC + M_{23}B_6] \rightarrow [FCC + M_{23}B_6 + Co(MoB)_2]$ for the amorphous (Fe, Co, Ni, Cr, Mo)-(B, C) alloy.

(3) For the as-cast rods, the glassy alloy with x = 25 shows the highest yield strength of 3500 MPa and Vickers hardness of 1240.

(4) The amorphous (Fe, Co, Ni, Cr, Mo)-(B, C) alloys show higher corrosion resistance with increasing B and C contents.

Further experiments, such as the tribological effect and adhesion testing, are necessary to explore the potential applications of the present HE alloys as a coating material, even though their good characteristics have already been reported for the (Fe, Cr, Mo)-(B, C) bulk glassy alloys.

Author Contributions: Conceptualization, A.I. and F.K.; Methodology, F.W. and C.C.; Validation, A.I. and C.C.; Experiments, F.K., F.W. and C.C.; Data curation, A.I. and F.W.; Writing—original draft preparation, F.K.; Editing and translation, A.I., F.W. and C.C.; Visualization, F.W. and F.K.; Project administration, A.I. and F.W. All authors have read and agreed to the published version of the manuscript.

Institutional Review Board Statement: Not applicable.

Informed Consent Statement: Not applicable.

Data Availability Statement: Dataset available on request from the authors.

Conflicts of Interest: The authors declare no conflict of interest.

References

1. Yang, M.; Liu, X.J.; Ruan, H.H.; Wu, Y.; Wang, H.; Lu, Z.P. High Thermal Stability and Sluggish Crystallization Kinetics of High-Entropy Bulk Metallic Glasses. *J. Appl. Phys.* **2016**, *119*, 245112. [CrossRef]
2. Li, Y.; Wang, S.; Wang, X.; Yin, M.; Zhang, W. New Fenicrmo(P, C, B) High-Entropy Bulk Metallic Glasses with Unusual Thermal Stability and Corrosion Resistance. *J. Mater. Sci. Technol.* **2020**, *43*, 32–39. [CrossRef]
3. Cantor, B.; Chang, I.T.H.; Knight, P.; Vincent, A.J.B. Microstructural Development in Equiatomic Multicomponent Alloys. *Mater. Sci. Eng. A* **2004**, *375–377*, 213–218. [CrossRef]
4. Ma, L.; Wang, L.; Zhang, T.; Inoue, A. Bulk glass formation of Ti-Zr-Hf-Cu-M (M = Fe, Co, Ni) alloys. *Mater. Trans.* **2002**, *43*, 277–280. [CrossRef]
5. Yeh, J.W.; Chen, S.K.; Lin, S.J.; Gan, J.Y.; Chin, T.S.; Shun, T.T.; Tsau, C.H.; Chang, S.Y. Nanostructured High-Entropy Alloys with Multiple Principal Elements: Novel Alloy Design Concepts and Outcomes. *Adv. Eng. Mater.* **2004**, *6*, 299–303. [CrossRef]
6. Zhou, Q.; Du, Y.; Han, W.; Ren, Y.; Zhai, H.; Wang, H. Identifying the Origin of Strain Rate Sensitivity in a High Entropy Bulk Metallic Glass. *Scr. Mater.* **2019**, *164*, 121–125. [CrossRef]
7. Yavari, A.R.; Lewandowski, J.J.; Eckert, J. Mechanical Properties of Bulk Metallic Glasses. *MRS Bull.* **2007**, *32*, 635–638. [CrossRef]
8. Takeuchi, A.; Inoue, A. Classification of Bulk Metallic Glasses by Atomic Size Difference, Heat of Mixing and Period of Constituent Elements and Its Application to Characterization of the Main Alloying Element. *Mater. Trans.* **2005**, *46*, 2817–2829. [CrossRef]
9. Chen, H.S.; Turnbull, D. Formation and Stability of Amorphous Alloys of Au-Ge-Si. *Acta Metall.* **1970**, *18*, 261–263. [CrossRef]
10. George, E.P.; Raabe, D.; Ritchie, R.O. High-entropy alloys. *Nat. Rev. Mater.* **2019**, *4*, 515–534. [CrossRef]
11. Arshad, M.; Amer, M.; Hayat, Q.; Janik, V.; Zhang, X.; Moradi, M.; Bai, M. High-Entropy Coatings (HEC) for High-Temperature Applications: Materials, Processing, and Properties. *Coatings* **2022**, *12*, 691. [CrossRef]
12. Suryanarayana, C.; Inoue, A. *Bulk Metallic Glasses*, 2nd ed.; CRC Press: Boca Raton, FL, USA, 2017.
13. Ding, H.Y.; Yao, K.F. High Entropy Ti$_{20}$Zr$_{20}$Cu$_{20}$Ni$_{20}$Be$_{20}$ Bulk Metallic Glass. *J. Non-Cryst. Solids* **2013**, *364*, 9–12. [CrossRef]
14. Jalali, A.; Malekan, M.; Park, E.S.; Rashidi, R.; Bahmani, A.; Yoo, G.H. Thermal behavior of newly developed Zr$_{33}$Hf$_8$Ti$_6$Cu$_{32}$Ni$_{10}$Co$_5$Al$_6$ high-entropy bulk metallic glass. *J. Alloys Compd.* **2022**, *892*, 162220. [CrossRef]
15. Qi, T.; Li, Y.; Takeuchi, A.; Xie, G.; Miao, H.; Zhang, W. Soft Magnetic Fe$_{25}$Co$_{25}$Ni$_{25}$(B, Si)$_{25}$ High Entropy Bulk Metallic Glasses. *Intermetallics* **2015**, *66*, 8–12. [CrossRef]
16. Kim, J.; Oh, H.S.; Kim, J.; Ryu, C.W.; Lee, G.W.; Chang, H.J.; Park, E.S. Utilization of High Entropy Alloy Characteristics in Er-Gd-Y-Al-Co High Entropy Bulk Metallic Glass. *Acta Mater.* **2018**, *155*, 350–361. [CrossRef]
17. Gong, P.; Wang, D.; Zhang, C.; Wang, Y.; Jamili-Shirvan, Z.; Yao, K.; Wang, X. Corrosion Behavior of TiZrHfBeCu(Ni) High-Entropy Bulk Metallic Glasses in 3.5 wt. % Nacl. *Npj Mater. Degrad.* **2022**, *6*, 77. [CrossRef]
18. Batalha, W.C.; Roche, V.; Champion, Y.; Mantel, M.; Verdier, M.; Martin, V.; Kiminami, C.S.; Junior, A.M.J. Newly-Developed Pseudo-High Entropy Amorphous Alloys: Structure/Microstructure Evolution, Mechanical and Corrosion Properties. *J. Non-Cryst. Solids* **2023**, *613*, 122369. [CrossRef]
19. Jin, Y.; Inoue, A.; Kong, F.L.; Zhu, S.L.; Al-Marzouki, F.; Greer, A.L. Icosahedral and Dodecagonal Quasicrystal Plus Glass Alloys with Plastic Deformability. *Acta Mater.* **2020**, *199*, 1–8. [CrossRef]
20. Sang, L.; Xu, Y. Amorphous Behavior of Zrxfenisi0.4b0.6 High Entropy Alloys Synthesized by Mechanical Alloying. *J. Non-Cryst. Solids* **2020**, *530*, 119854. [CrossRef]

21. Tsai, P.-H.; Lee, C.-I.; Song, S.-M.; Liao, Y.-C.; Li, T.-H.; Jang, J.S.-C.; Chu, J.P. Improved Mechanical Properties and Corrosion Resistance of Mg-Based Bulk Metallic Glass Composite by Coating with Zr-Based Metallic Glass Thin Film. *Coatings* **2020**, *10*, 1212. [CrossRef]
22. Zhang, J.; Li, J.; Jing, M.; Zhao, L.; Qi, Y.; Yang, W.; Wang, X. The Effect of Electroplating Nickel on the Mechanical Properties of Brittle Mg-Based Bulk Metallic Glasses. *Coatings* **2023**, *13*, 1598. [CrossRef]
23. Yoon, S.; Kim, J.; Bae, G.; Kim, B.; Lee, C. Formation of coating and tribological behavior of kinetic sprayed Fe-based bulk metallic glass. *J. Alloys Compd.* **2011**, *509*, 347–353. [CrossRef]
24. Madge, S.V.; Greer, A.L. Laser additive manufacturing of metallic glasses: Issues in vitrification and mechanical properties. *Oxf. Open Mater. Sci.* **2021**, *1*, itab015. [CrossRef]
25. Cieslak, J.; Tobola, J.; Berent, K.; Marciszko, M. Phase composition of Al_xFeNiCrCo high entropy alloys prepared by sintering and arc-melting methods. *J. Alloys Compd.* **2018**, *740*, 264–272. [CrossRef]
26. Mondal, K.; Murty, B.; Chatterjee, U. Electrochemical behavior of multicomponent amorphous and nanocrystalline Zr-based alloys in different environments. *Corros. Sci.* **2006**, *48*, 2212–2225. [CrossRef]
27. Louzguine-Luzgin, D.V.; Bazlov, A.I.; Ketov, S.V.; Greer, A.L.; Inoue, A. Crystal Growth Limitation as a Critical Factor for Formation of Fe-Based Bulk Metallic Glasses. *Acta Mater.* **2015**, *82*, 396–402. [CrossRef]
28. Oyen, M.L.; Cook, R.F. A Practical Guide for Analysis of Nanoindentation Data. *J. Mech. Behav. Biomed. Mater.* **2009**, *2*, 396–407. [CrossRef] [PubMed]
29. Detrois, M.; Pei, Z.; Rozman, K.A.; Gao, M.C.; Poplawsky, J.D.; Jablonski, P.D.; Hawk, J.A. Partitioning of Tramp Elements Cu and Si in a Ni-Based Superalloy and Their Effect on Creep Properties. *Materialia* **2020**, *13*, 100843. [CrossRef]
30. Ruf, R.R.; Tsuei, C.C. Extremely High Corrosion Resistance in Amorphous Cr–B Alloys. *J. Appl. Phys.* **1983**, *54*, 5705–5710. [CrossRef]
31. Guo, S.; Liu, C.T. Phase Stability in High Entropy Alloys: Formation of Solid-Solution Phase or Amorphous Phase. *Prog. Nat. Sci. Mater. Int.* **2011**, *21*, 433–446. [CrossRef]
32. Wang, Z.; Zhang, S. Research and Application Progress of High-Entropy Alloys. *Coatings* **2023**, *13*, 1916. [CrossRef]
33. Cemin, F.; Artico, L.L.; Piroli, V.; Yunes, J.A.; Figueroa, C.A.; Alvarez, F. Superior in Vitro Biocompatibility in Nbtativzr (O) High-Entropy Metallic Glass Coatings for Biomedical Applications. *Appl. Surf. Sci.* **2022**, *596*, 153615. [CrossRef]
34. Li, H.F.; Zheng, Y.F. Recent Advances in Bulk Metallic Glasses for Biomedical Applications. *Acta Biomater.* **2016**, *36*, 1–20. [CrossRef]